submitted to THE ASTROPHYSICAL JOURNAL LETTERS, 05/04/99

arXiv:astro-ph/9908097v2 14 Jan 2000

ANALYSIS OF TEMPORAL FEATURES OF GAMMA-RAY BURSTS IN THE INTERNAL SHOCK MODEL

M. SPADA[1,2], A. PANAITESCU[1] & P. MÉSZÁROS [1]
Department of Astronomy & Astrophysics, Pennsylvania State University, University Park, PA 16802

ABSTRACT

In a recent paper we have calculated the power density spectrum of Gamma-Ray Bursts arising from multiple shocks in a relativistic wind. The wind optical thickness is one of the factors to which the power spectrum is most sensitive, therefore we have further developed our model by taking into account the photon down-scattering on the cold electrons in the wind. For an almost optically thick wind we identify a combination of ejection features and wind parameters that yield bursts with an average power spectrum in agreement with the observations, and with an efficiency of converting the wind kinetic energy in 50–300 keV emission of order 1%. For the same set of model features the interval time between peaks and pulse fluences have distributions consistent with the log-normal distribution observed in real bursts.

Subject headings: gamma-rays: bursts - methods: numerical - radiation mechanisms: non-thermal

1. INTRODUCTION

The Gamma-Ray Burst (GRB) light-curves are complex and irregular, without any systematic temporal features (Fishman & Meegan 1995) and an understanding of the origin of the temporal behavior of GRBs remains an open issue. Statistical studies are necessary in order to identify the physical properties of the emission mechanism existent in all or a group of GRBs. Recently Beloborodov et al. 1998, hereafter BSS98, have used the Fourier analysis of a sample of long GRB light-curves to study the statistical properties of their power density spectra (PDS). The PDS features together with other temporal properties of the observed GRBs, such as the distributions of the time interval between peaks and of the pulse fluence (McBreen et al. 1994, Li & Fenimore 1996), can be used to constrain the physical characteristics of the GRB source.

In the framework of the internal shock model, the rapid variability and complexity of the GRB light-curves is due to the emission from multiple shocks in a relativistic wind (Rees & Mészáros 1994, Kobayashi et al. 1997, Daigne & Mochkovitch 1998). The ejecta are released by the source during a time comparable to the observed burst duration. The instability of the wind leads to shocks which convert a fraction of the bulk kinetic energy in internal energy at a distance $R \sim 10^{12}-10^{14}$ cm from the central engine. A turbulent magnetic field is generated and electrons are shock-accelerated, leading to synchrotron emission and inverse Compton scatterings. Within the framework of the internal shock model an alternative hypothesis about the particle acceleration and radiation emission is the quasi-thermal Comptonization proposed by Ghisellini & Celotti (1999), in which particles are re-accelerated for all the duration of the collision.

In this paper we analyze the features of the GRB light-curves arising from internal shock model, in order to identify the parameters that affect most strongly the GRB emission (§2). By comparing the features of the simulated bursts with the observed burst PDS and the distributions of the interval time between peaks and of the pulse fluence, we constrain some of the physical properties of the ejecta.

2. OUTLINE OF THE MODEL

We simulate GRB light-curves by adding pulses radiated in a series of internal shocks that occur in a transient, unstable relativistic wind. As we showed in PSM99 the observed burst variability time-scale depends mostly on the wind dynamics, its optical thickness and its radiative efficiency in the BATSE window. Here we model the wind dynamics and the emission processes as in PSM99, but we include a more accurate treatment of the photon down-scattering on the cold electrons in the wind. We calculate the effect of the photon diffusion through the colliding shells and the wind on the pulse duration and on the energy of the emergent photon, rather than just attenuating the pulse fluence according to the optical thickness of the wind through which it propagates. However the contribution of these photons to the duration of the received pulses may be important for bursts that are not very optically thin, and the photon down-scattering should be taken into account for more reliable calculations of GRB light-curves.

As described in PSM99, the wind is discretized as a sequence of $N = t_w/t_v$ shells, where t_w is the duration time of the wind ejection from the central source and $t_v << t_w$ is the average interval between consecutive ejections. The shell Lorentz factors Γ_i are random between Γ_m and Γ_M, where Γ_M can be constant during t_w ("uniform wind") or modulated on time scale $\lesssim t_w$ ("modulated wind"). The shell mass M_i is drawn from a log-normal distribution with an average value $\overline{M} = M_w/N$ and a dispersion $\sigma_M = \overline{M}$, where M_w is the total mass in the wind, allowing thus the occasional ejection of very massive shells. The total mass is determined by requiring that $\sum_{i=1}^{N} M_i\Gamma_i c^2 = L_w t_w$ where L_w is the wind luminosity. The time interval Δt_i between two consecutive ejections i and $i+1$ is proportional to the i-th shell energy, resulting in a wind luminosity constant throughout the entire wind, and equal to a pre-set value L_w. This implies that more energetic shells are

[1] also Institute of Theoretical Physics, University of California, Santa Barbara

[2] also Dipartimento di Astronomia e Scienza dello Spazio, Università degli studi di Firenze, Italy

followed by longer "quiet" times, during which the "central engine" replenishes.

Given the wind ejection, we calculate the radii where internal collisions take place and determine the emission features for each pulse: observer frame duration, fluence, and photon arrival time T_{ob}, accounting for relativistic and cosmological effects. The peak photon flux for each pulse is calculated assuming the pulse shape that Norris et al. (1996) identified in the real bursts, described by a two-sided exponential function. The addition of all the pulses, as seen by the observer in the 50–300 keV range (the $2^{\rm nd}$ and $3^{\rm rd}$ BATSE channels) gives the burst γ-ray light-curve, that is binned on time-scale of 64 ms and is used for the computation of the power spectrum.

For each collision there is a reverse (RS) and a forward shock (FS). The shock jump equations allow the calculation of the physical parameters of the shocked fluids (Panaitescu & Mészáros 1999), determine the velocity of these shocks v_{sh}, the compression ratio, the thickness Δ of the merged shell at the end of the collision, and the internal energy in the shocked fluid U'_s (primed quantities are measured in the co-moving frame). The accelerated electrons - a fraction ζ_e of the total number - have a power-law distribution of index $-p$, starting from a low Lorentz factor γ_m. Assuming that the energy stored in electrons is a fraction ϵ_e of the internal energy, we calculate γ_m (see PSM99). The magnetic field B is parameterized through the fraction ϵ_B of the internal energy it contains: $B^2 = 8\pi\epsilon_B U'_s$. We assume that between two consecutive collisions the thickness of the shell increases proportionally to the fractional increase of its radius $d\Delta/\Delta \propto dR/R$. The shell internal energy increases in each collision by the fraction of U'_s that is not radiated, and decreases during the expansion due to adiabatic losses.

The shock-accelerated electrons radiate and the emitted photons can be up-scattered on the hot electrons ($\gamma_e >> 1$) or down-scattered by the cold ones ($\gamma_e \approx 1$). Far from the Klein-Nishina regime the optical depth to up-scattering is $\tau_{ic} = \sigma_{Th}\zeta_e n'_e \min(ct'_\gamma, \Delta')$, where n'_e is the co-moving electrons density and $t'_\gamma = t'_{sy}/(1+y)$ is the radiative time scale, with t'_{sy} the synchrotron cooling time and y the Comptonization parameter (for $\tau_{ic} < 1$, $y = \gamma_m^2\tau_{ic}$). The optical thickness τ_c for the cold electrons within the emitting shell is evaluated by taking into account the cold electrons within the hot fluid, those that were accelerated but have cooled radiatively while the shock crossed the shell, and those within the yet un-shocked part of the shell.

A fraction $\min(1, \tau_{ic})$ of the synchrotron photons is inverse Compton scattered $n_{ic} = \max(1, \tau_{ic}^2)$ times, unless the Klein-Nishina regime is reached. The energy of the up-scattered photon and the ratio of the Compton to synchrotron power can be cast in the forms:

$$h\nu_{ic} = \min\left[\gamma_m m_e c^2, \left(\frac{4}{3}\gamma_m^2\right)^{n_{ic}} h\nu_{sy}\right] , \qquad (1)$$

$$\frac{P_{ic}}{P_{sy}} = \min\left\{\gamma_m \frac{m_e c^2}{h\nu_{sy}}, \left[\frac{4}{3}\gamma_m^2 \min(1, \tau_\zeta)\right]^{n_{ic}}\right\} , \qquad (2)$$

which take into account the upper limits imposed by the Klein-Nishina effect. Figure $1c$ shows the evolution of the synchrotron and inverse Compton peak energies during the wind expansion: the energy is lower for larger collisions radii, due to the increased shell volume and the less relativistic shocks, which lead to lower magnetic fields and electron random Lorentz factors.

The duration δT_0 of the emitted pulse (i.e. ignoring the diffusion through optically thick shells) is determined by (1) the spread in the photons arrival time $\delta T_\theta \approx R/(2\Gamma^2 c)$ due to the geometrical curvature of the emitting shell, (2) the shock shell-crossing time $\delta T_\Delta = \Delta/|v_{sh} - v_0|$, (where v_0 is the shell pre-shock flow velocity), and (3) the radiative cooling time $\delta T_\gamma \approx t'_\gamma/\Gamma$, which we add in quadrature to determine δT_0. As shown in Figure 1b, all these time scales increase on average with radius: δT_θ is proportional to R, δT_Δ increases due to the continuous widening of the shell, and δT_γ is longer for later collisions because γ_m and B are lower. For $\zeta_e = 1$, $\epsilon_e \approx 0.25$ and $\epsilon_B \approx 0.1$ the radiative cooling time is negligible respect to δT_θ and δT_Δ for collisions occurring at $R < 5 \times 10^{14}$ cm, while for larger radii δT_γ is the dominant contribution to the pulse duration (Figure 1b). For the assumed linear shell broadening between consecutive collisions we find numerically that the angular spread and shock-crossing times are comparable during the entire wind expansion.

The optical thickness τ_c is mainly determined by the wind luminosity L_w and the range of Lorentz factors in the wind. In Figure $1a$ for $30 < \Gamma < 1000$ and $L_w = 10^{53}\,{\rm erg\,s^{-1}}$ most collisions occur at $R = 5 \times 10^{13}$ – 10^{15} cm where the emitting shells are optically thin. For lower Lorentz factors ($5 < \Gamma < 300$) the collisions take place at smaller radii ($R = 10^{12} - 10^{13}$ cm) and the wind is optically thick (Figure $1d$). When $\tau_c > 1$ photons are down-scattered by the cold electrons before they escape the emitting shell, leading to a decrease in the photon energy and an increase of the pulse duration. For down-scatterings occurring in the Thomson limit ($\varepsilon' \ll m_e c^2/\gamma_e$) the energy of the emergent photon can be approximated by $\varepsilon'_{ds} = \varepsilon'(1 - \varepsilon'/m_e c^2)^{\tau_c^2}$, where τ_c^2 is the average number of scatterings suffered by a photon. For more energetic photons, we evaluate ε'_{ds} numerically, because the cross section depends on the photon energy and changes after each photon-electron interaction. For the set of parameters considered in this paper, the Thompson limit is usually a good approximation to treat the down-scattering of the synchrotron photons during all the wind expansion. For the smaller collision radii the inverse Compton emission peaks at large comoving frame energies and the general case has to be considered. Figure $1f$ shows the evolution of the synchrotron and inverse Compton observer frame peak energies for a thick wind. At $R \approx 10^{12}$ cm, $\tau_c \approx 10^3$ and the ~ 10 keV synchrotron emission is down-scattered by an order of magnitude, while ~ 100 MeV inverse Compton radiation is down-scattered to ≈ 10 keV.

We approximate the increase in the pulse duration due to the diffusion through optically thick shells by the time δT_d it takes to a photon to diffuse through them, which we add to δT_0 to determine the observed pulse duration δT. In the Thompson limit $\delta T_d \approx 5\tau_c\Delta/(24c)$; in the general case the diffusion time is given by $\delta T_d = \left\{\sum_{i=1}^{n_s}[\tau(\varepsilon'_i)]^{-1}\right\}\Delta/(2c)$, where $\tau(x_i)$ is the optical thickness for the i-th scattering and n_s is the number of down-scatterings on the cold electrons, evaluated requiring the photon random walk equal to the shell width. Figure $1e$ shows the evolution of the pulse duration during the wind expansion: for smaller collision radii $\delta T_d > \delta T_0$ and the pulse duration is determined by δT_d which decreases with R. For larger radii $\delta T_d < \delta T_0$, thus $\delta T \approx \delta T_0$ and increases with R.

For a given pulse, we add to the pulse duration the diffusion time it takes the photon to propagate through all the shells of optical thickness above unity. As shown in Figure $1d$, the wind optical thickness is 1–2 orders of magnitude smaller than the

optical thickness of the emitting shell (τ_c). Nevertheless the photon diffusion through the optically thick shells in the wind can contribute up to 30% to the pulse duration because of the broadening of the shell width during the wind expansion.

The 30–500 keV pulse energy is a fraction of the kinetic energy of the colliding shells, equal to the product of the dynamical (ϵ_d), the radiative (ϵ_r), and the window efficiency (ϵ_w).

1) The *dynamical efficiency* is the fraction of the kinetic energy that is converted to internal, and is given by the energy and momentum conservation in the collision of a forward shell (M_f, Γ_f) caught up by a back shell (M_b, $\Gamma_b > \Gamma_f$):

$$\epsilon_d = 1 - \frac{M\Gamma}{\Gamma_b M_b + \Gamma_f M_f} \tag{3}$$

where $M = M_b + M_f$ is the total mass and

$$\Gamma = \left[\frac{\Gamma_b M_b + \Gamma_f M_f}{M_b/\Gamma_b + M_f/\Gamma_f}\right]^{1/2} \tag{4}$$

is the final Lorentz factor of the merged shell. The ϵ_d decreases with Γ_b/Γ_f and is maximized by $M_b = M_f$, so the inner collisions, for which the difference in the shells Lorentz factor is larger, are the most dynamically efficient, with $\epsilon_d \gtrsim 0.1$. During the wind expansion the collisions diminish the initial difference in the Lorentz factors and the dynamical efficiency decreases to 1% or less. As show in the next section, a modulation in the ejection Lorentz factor is necessary to dynamically efficient collisions at larger radii.

2) The *radiative efficiency* is the fraction of the internal energy converted in radiation, and is given by:

$$\epsilon_r = \epsilon_e \frac{t_\gamma^{-1}}{t_\gamma^{-1} + t_{ad}^{-1}} \tag{5}$$

where $t_{ad} \sim R/c$ is the adiabatic time-scale. The radiative efficiency decreases during the wind expansion and it's upper limit is the fraction ϵ_e of internal energy stored in electrons. For magnetic fields not too far from equipartition, the radiative timescale is determined by the synchrotron losses.

3) The *window efficiency* is the fraction of the radiated energy that arrives at observer in the 50–300 keV band. The calculation of ϵ_w is based on the approximation of the synchrotron spectrum by three power-laws, with breaks at the cooling frequency ν_c and the peak frequency ν_{sy} (at which the γ_m-electrons radiate). If the $\nu_c < \nu_{sy}$ then the shape of the spectrum is given by:

$$F_\nu \propto \begin{cases} \nu^{1/3} & \nu < \nu_c \\ \nu^{-1/2} & \nu_c < \nu < \nu_{sy} \\ \nu^{-p/2} & \nu_{sy} < \nu \end{cases}, \tag{6}$$

where p is the index of the assumed power-law electron distribution. If $\nu_{sy} < \nu_c$ then

$$F_\nu \propto \begin{cases} \nu^{1/3} & \nu < \nu_{sy} \\ \nu^{-(p-1)/2} & \nu_{sy} < \nu < \nu_c \\ \nu^{-p/2} & \nu_c < \nu \end{cases}. \tag{7}$$

The inverse Compton spectrum has the same shape but is shifted to higher energy by the factor implied by equation (1). For optically thick emitting shells we approximate the burst spectrum as given in equations (6) and (7), using the down-scattered cooling and peak frequencies.

3. EFFECT OF THE PHYSICAL PARAMETERS ON THE GRB POWER DENSITY SPECTRUM

In this section we analyze the effect of the model parameters on two distributions that characterize the GRB temporal structure: the PDS and the distribution of the interval δ_p between peaks. The relevant model parameters describe the wind ejection (t_v, t_w, Γ_{min}, Γ_{max} and L_w) and the energy release (ϵ_e, ζ_e and ϵ_B). In order to diminish the large PDS fluctuations, in this section we use power spectra that are averaged over 10 peak-normalized bursts. The light-curve peaks are identified with the peak finding algorithm (PFA) described by Li & Fenimore (1996). For each time bin T_p with a photon flux C_p higher than those of the neighboring time bins, we search for the times $T_1 < T_p$ and $T_2 > T_p$ when the photon fluxes C_1 and C_2 satisfy $C_p - C_{1,2} > N_{var}\sqrt{C_p}$. A peak is identified at T_p there are no time bins between T_1 and T_2 with photon fluxes higher than C_p. The light-curve valleys are identified as the minima between two consecutive peaks.

The energy release parameters ϵ_e, ζ_e, and ϵ_B determine the 50–300 keV radiative efficiency of the pulses. In an optically thin wind, the parameter that affects mostly the window efficiency is the electron injection fraction ζ_e (for an optically thick wind the photons are down-scattered before they escape the shells and the window efficiency depends also on τ_c). Figures 2a and 2b show the PDS and the δ_p distributions for a thin wind with $L = 10^{52}\,\mathrm{erg\,s^{-1}}$, $\Gamma_m = 30$, and $\Gamma_M = 800$, and for two different ζ_e (1 and 10^{-3}). In both cases synchrotron emission is the dominant radiative process the inverse Compton contribution to the total emission being 10% for $\zeta_e = 1$ and less then 0.1% for $\zeta_e = 10^{-3}$. For $\zeta_e = 1$ the synchrotron emission lies mainly below the BATSE window (Figure 2c), the window efficiency decreases from shorter to longer pulses, the light-curve is formed by pulses with a duration of $\delta T \approx 10^{-2}$ s, and with an average difference in the photon arrival time $\Delta T \approx 0.2$ s. Because $\Delta T \gg \delta T$, the distribution of intervals between peaks is determined by the pulses arrival times and peaks at 0.1 – 0.2 s. If $\zeta_e = 10^{-3}$ the synchrotron emission is above the BATSE window for $\delta T < 0.3$s and the window efficiency is maximized for $\delta T \approx 0.2$ – 0.4 s. The light curve is formed by longer pulses, the lower frequency power in the PDS increases and the interval time between peaks shifts to longer time-scale.

The 50–300 keV efficiency of the synchrotron and the inverse Compton emissions is determined by the strength magnetic field B. While for $\epsilon_B > 0.1$ the emission is dominated by synchrotron radiation, for values of the magnetic field well below equipartition ($\epsilon_B < 0.01$) the burst emission is dominated by the inverse Compton. Because the shape of the PDS does not change, we conclude that the PDS is not sensitive to ϵ_B and the relative contribution of synchrotron and inverse Compton in the light-curve.

The ejection parameters determine the dynamics of the wind and the evolution of the pulse dynamical efficiency ϵ_d. The latter reflects the evolution of the differences between the Lorentz factors of a pair of colliding shells. The first collisions remove the initial random differences, and the merged shells have Lorentz factors near the ejection average value $\overline{\Gamma} = (\Gamma_m + \Gamma_M)/2$. If the wind is uniform $\overline{\Gamma}$ is the same for all the shells, resulting in a steady decrease of ϵ_d during the wind expansion. If the range of shell ejection Lorentz factors is variable on time scale of the order of t_w (a "modulated" wind), $\overline{\Gamma}$ reflects the

initial modulation in Γ_M and large radii collisions that are dynamically efficient are still possible.

Figure 3a shows the effect on the PDS of square-sine modulations of the upper limit Γ_M with periods $P = t_w$ and $P = t_w/4$. The i-th shell ejection Lorentz factor is given by

$$\Gamma_i = \Gamma_m + a_i \sin^2\left(\frac{\omega i}{N}\right)(\Gamma_M - \Gamma_m), \quad (8)$$

where a_i is a random number between 0 and 1, and $\omega = 2\pi t_w/P$. The modulation shifts the power from high to low frequencies, and the magnitude of this shift depends on the modulation period. If $P = t_w$ the effect of the modulation for interaction radii less than $\approx 10^{14}$ cm (corresponding to $\delta T \approx 1$ s) is negligible and the wind evolves as in the uniform case: the ϵ_d decreases from 5% to 0.2% when δT increases from 0.01 s to 1 s (Figure 3c). For $R \gtrsim 10^{14}$ cm the modulation becomes relevant: the wind is formed of groups of few massive shells with different Lorentz factors. The dynamical efficiency remains constant for subsequent collisions between massive shells, which yield long pulses ($\delta T = 0.3 - 10$ s) that carry a substantial fraction of the total burst fluence.

Figure 3d shows that the dependence on δT of the synchrotron efficiency ϵ_{sy} of the FS pulses has a similar behavior as that of ϵ_d, because the internal energy density in the shocked plasma depends on ϵ_d. For an higher internal energy, the minimum electron Lorentz factor γ_m increases, leading to a higher energy emission and a shorter radiative cooling timescale. Therefore the synchrotron efficiency remains constant on the same range of δT where is constant the dynamical efficiency, contributing to a shift of power to low frequencies in the PDS.

The optical thickness of the wind depends mostly on the range of shell Lorentz factors ($\Gamma_m - \Gamma_M$) and on the wind luminosity (L_w). Figure 4a shows PDSs for two ranges of Lorentz factors, 30–1000 and 10–150. In the former case the wind is essentially optically thin, and the photon diffusion does not affect the pulses duration δT, that increases with R (Figure 4c) from 0.01 s to 1 s, between 10^{13} and 10^{15} cm. In the latter case the wind is optically thick, in 80% of the collisions $\tau_c > 1$, and the pulse duration is given by the diffusion time: δT_d decreases from ≈ 5 s to ≈ 0.6 s between $R = 3 \times 10^{12}$ cm and $R = 10^{13}$ cm, where δT is determined mainly by the shell curvature and thus increases with R. For the optically thick wind the long pulses are generated at smaller R where the efficiency has the maximum value, and the pulse energy increases with δT (Figure 4d). The PDS has more power at low frequency and the time intervals between peaks are longer than in the optically thin case (Figure 4b). The 50–300 keV efficiency is of the same order for the two cases: 4×10^{-3} and 5×10^{-3} for a range of Lorentz factors of 30–1000 and 10–150, respectively.

An increase in the wind luminosity has a similar effect on the PDS shape as a decrease in Γ_m and Γ_M. In the latter case the wind becomes thicker because the shells are more massive.

The variability time scale t_v affects the dynamical evolution of the shells in the following way. If the time intervals between successive ejections delays decreases then the collisions occur at smaller radii, where the wind is more optically thick. The differences between the Lorentz factors diminish faster (there are more shells for smaller t_v), reducing the dynamical efficiency for short pulses. For the modulated wind this effect is more relevant than in the random case. The duration t_w of the wind ejection determines mainly the number of shells, and changes in t_w do not affect much the evolution of uniform winds. However, for a modulated wind, t_w also determines the number of periods in the Lorentz factor (if the duration of a period is independent of t_w), influencing thus the clumping of shells.

The burst redshift determines the co-moving energy range which is redshifted into the observing range, leading to a change in the total pulse efficiency, and altering the observed pulse duration. Obviously, by increasing the burst redshift, power is shifted from higher to lower frequencies.

4. COMPARISON WITH THE OBSERVATIONS

An analysis of the PDS of real bursts was presented by BSS98. They calculated the Fourier transform of 214 long ($T_{90} > 20$ s) and bright burst, and have found that the average PDS is a power-law ($P_f \propto f^{-5/3}$, f is frequency) over almost two orders of magnitude in frequency, between 0.02 Hz and 2 Hz, where a break is observed, indicating a paucity of pulses with duration less than ≈ 0.5 s. The distribution of intervals between peaks has been studied by McBreen et al. (1994) and by Li & Fenimore (1996), who showed that the distributions of the pulse fluence S_p and of the time interval δ_p between peaks are consistent with a log-normal distribution.

As was shown in the previous section, if the wind is optically thin and the ejection features are random, the pulse duration increases with the collision radius and the emission efficiency decreases during the wind expansion. The short inner collisions yield most of the 50–300 keV burst emission and the internal shock model predicts a flat PDS with equal power at low and high frequency. Thus, in order to explain the observed behavior, we need a configuration of the parameters which shifts power from the short to the long time-scales in the light-curves. Moreover, the δ_p distribution is not log-normal: Figures 2b, 3b, and 4b show that in GRBs arising from optically thin, uniform winds there are too many short intervals between peaks respect to a Gaussian $\log \delta_p$ distribution.

PSM99 have identified three possible ways to explain the deficit of pulses with $\delta T < 1$ s:

(1) a reduction in the electron injection fraction. This increases the photon energy, reducing the window efficiency of the short pulses (causing the high energy break) and increasing that of the longer ones. However the behavior of the PDS at lower frequency remains flat (see Figure 2a).

(2) a modulation of the shell ejection Lorentz factor. This allows different configurations for the collisions series and a higher dynamical efficiencies for longer pulses (see Figure 3a).

(3) an increase of the optical thickness of the wind. In this case the down-scattering suffered by the photons as they propagate through the wind increases the pulse duration for the small radii collisions, which yield the shorter duration pulses (see Figure 4a).

In Figure 5a we show a simulated light-curve for a square-sine modulated wind (with $P = t_w$) The burst 50–300 keV efficiency is 1%, and the 90% of the RS and 80% of the FS propagate in optically thick shells. If $N_{var} = 0.1$ (the free parameter of the PFA), we find 22 pulses in the light-curve shown in Figure 5a. In order to have more peaks we simulate four light-curves with the same injection features and wind parameters and we calculate the interval between peaks δ_p (Figure 5b) and peak fluence S_p (Figure 5c) distributions. The distributions are similar to a log-normal one, and the choice of N_{var} does not affect strongly their shape.

In order to compare the PDS of the simulated bursts with the observed one, we consider an ensemble of cosmological GRBs. Some authors (Totani, 1997, Wijers, et al. 1998, Krumholz et al. 1998, Hogg & Fruchter 1999, Mao & Mo 1999) have used a GRB co-moving rate density proportional to the star formation rate. Others (Reichart & Mészáros 1997) have employed a power-law GRB density evolution with redshift, which was found by (Bagot et al. 1998) to be consistent for $z \lesssim 2$ with their results from population-synthesis computations of binary neutron stars merger rates. Finally, other researchers (Krumholz et al. 1998, Hogg & Fruchter 1999), have considered a constant GRB rate density. In this work, we use the power-law with redshift GRB density evolution $n_c(z) \propto (1+z)^D$, mainly as a convenient parameterization. An $n_c(z)$ proportional to the star formation rate would lead to different sets of model parameters (see below), but the differences are minor, because the two functions differ substantially in shape only for $z > 1$, where there is a strong decrease of the co-moving volume per unit redshift and a smaller chance of obtaining a burst that has a 50–300 keV peak photon flux below $1\,\gamma\,\mathrm{cm}^{-2}\mathrm{s}^{-1}$ (bursts dimmer than this limit are not included in the calculation of the average PDS and intensity distribution).

Given the rate density evolution, the GRB redshift is chosen from a probability distribution

$$\frac{d\mathcal{P}}{dz} \propto \frac{n_c(z)}{1+z}\frac{dV}{dz}\ , \tag{9}$$

where dV/dz is the cosmological co-moving volume per unit redshift

$$\frac{dV}{dz} = 4\pi\left(\frac{c}{H_0}\right)^3 \frac{[q_0 z - (1-q_0)(\sqrt{2q_0 z+1}-1)]^2}{q_0^4(2q_0 z+1)^{1/2}(1+z)^6}\ . \tag{10}$$

We assume $q_0 = 0.5$ and $H_0 = 75\,\mathrm{km\,s^{-1}Mpc^{-1}}$.

The inferred isotropic 50–300 keV luminosities of the GRBs that have measured redshifts span more than one order of magnitude, therefore the standard candle approximation is not a good approximation. We use an un-evolving power-law distribution for the wind luminosity:

$$\Phi(L) \propto L^{-\beta}\ , \quad L_m \le L \le L_M\ , \tag{11}$$

and zero otherwise. Note that this not the same as assuming that GRBs have a power-law distribution of their 50–300 keV luminosities, as it is usually done (e.g. Reichart & Mészáros (1997), Krumholz et al. 1998, Mao & Mo 1999), as the relationship between the wind and the 50–300 keV luminosities is set by the window efficiency (at the source) and, in the case of winds that are optically thick, by the wind optical thickness, both of which are dependent on the wind luminosity.

In finding model parameters that yield bursts consistent with the observations, we held constant $t_v = 25$ ms, $L_M/L_m = 100$, $\beta = 2$, $\varepsilon_e = 0.25$, $\varepsilon_B = 0.1$, and $p = 2.5$. The chosen t_v is short enough to ensure that the observed 2 Hz PDS break frequency is below $[(1+z)t_v]^{-1}$ (bursts with $z > 3$ are rarely brighter than $1\,\gamma\,\mathrm{cm}^{-2}\mathrm{s}^{-1}$), corresponding to the pulses that are partly suppressed by the choice of t_v. the PDS frequencies affected by the assumed $t_v = 25$ ms are $\gtrsim 10$ Hz. This may suggest a possible explanation for the PDS break observed by BSS98: the lack of pulses shorter than ~ 1 s is due to the existence of a minimum wind variability time-scale of the same order. However, such t_v's would be much larger than the dynamical time-scales of plausible GRB progenitors (Mészáros et al 1999), and we do not consider this a viable possibility. The choices of L_M/L_m and β are consistent with the values found by Reichart & Mészáros (1997), Mao & Mo (1999), and Krumholz et al. (1998) from fits to the observed intensity distribution. The values chosen for ε_e and ε_B are not too far from those determined by Wijers & Galama (1999) from the emission features of the afterglows of GRB 970508 and 971214. The above value of electron index p is close to the values implied by the observed slopes of the afterglow optical decays.

Figure 6b shows a burst-averaged PDS whose features are similar to that found by BSS98 in real bursts. The wind ejection is modulated by a square sine (eq. [8]) with a random period between $t_w/4$ and t_w. About 40% of the 300 simulated bursts have peak photon fluxes brighter than $1\,\gamma\,\mathrm{cm}^{-2}\mathrm{s}^{-1}$. Taking into account that the average redshift for these bursts is $\overline{z} = 0.90$ the average burst duration $\overline{T}_b \approx 1.5(1+\overline{z})t_w$ is close to the value $\overline{T}_b = 80$ s of the bursts used by BSS98 (the factor 1.5 was determined numerically and represents the ratio between the burst duration at the source redshift and t_w). As can be seen in Figure 6b, $P_f \propto f^{-5/3}$ between 0.04 Hz and 2 Hz and falls off steeper at frequencies larger than 2 Hz. The model parameters that led to the PDS of Figure 6b yield bursts whose integral intensity distribution is shown in Figure 6a, which consistent with the distribution found by Pendleton et al. (1996): excluding the bursts dimmer than $1\,\gamma\,\mathrm{cm}^{-2}\mathrm{s}^{-1}$, the model has $\chi^2 = 9.5$ for 9 degrees of freedom.

5. CONCLUSION

We have calculated power density spectra of GRBs arising from internal shocks in an unsteady relativistic wind. By studying how the features of these spectra depend on the model parameters (Figures 2, 3, and 4), we have identified a set parameters (Figure 6) that leads to bursts whose average PDS exhibits an $f^{-5/3}$ behavior (where f is frequency) for $0.04\,\mathrm{Hz} < f < 2\,\mathrm{Hz}$, as found by BSS98 in real GRBs. Moreover, the integral intensity distribution of the simulated bursts is consistent with that observed by Pendleton et al. (1996), and the distributions of the time intervals between peaks and of the pulse fluences are consistent with the log-normal distributions identified by Li & Fenimore (1996) in real bursts.

The characteristics of the modeled bursts with the above mentioned features are: (1) a sub-unity electron injection fraction, required to increase the radiative efficiency of the larger collision radii, (2) a modulated Lorentz factor of the ejected shells, necessary to increase the dynamical wind efficiency during the wind expansion and, (3) a shells optical thickness to scattering on cold electrons above unity, required to increase the duration of the pulses as they propagate through the colliding shells and the wind.

In the internal shock model, the most efficient collisions, with a dynamical efficiency of 10-20% and a radiative efficiency of $10-30\%$, happen in the first part of the wind expansion where the wind optically thickness is higher and the angular spread time, the shell shock-crossing time and the electrons cooling time are shorter ($\ll 0.5$ s). In order to reproduce the observed break at 2 Hz in the PDS, we have previously (see PSM99) attenuated the fluence of these short pulses according to an high wind optically thickness, with a resulting low burst efficiency (10^{-4} for an uniform wind and 10^{-3} for a modulated one). The study of the photon diffusion, presented here,

allowed us to find model parameters that yield an 1% efficiency of converting the wind kinetic energy into 50–300 keV emission. For an optically thick wind, the pulse duration of the first, efficient collisions at small radii is determinated by the time the photons take to escape the shells, that depends only on the colliding shells width and optically thickness τ_c. If $\tau_c \gg 1$ the diffusion time for the efficient collisions is $\gtrsim 0.5$ s and the simulated average PDS shows the break at 2 Hz with a burst efficiency close to the maximal value (few %) admitted by the model (see also Kumar 1999).

This research is supported by NASA NAG5-2857, NSF PAY94-07194 and the CNR. We are grateful to Martin Rees, Stein Sigurdsson and Marco Salvati for stimulating comments.

REFERENCES

Bagot, P., Portegies Zwart, S.F., & Yungelson, L.R. 1998, A&A, 332, L57
Beloborodov, A.M., Stern, B.E., & Svensson, R. 1998 (BSS98), ApJ, 508, L25
Daigne, F. & Mochkovitch, R., 1998, MNRAS, 296, 275
Fishman, G.J. & Meegan, C.A. 1995, ARAA, 33, 415
Ghisellini, G. & Celotti, A. 1999, ApJ, 511, L93
Hogg, D.W. & Fruchter, A.S. 1999, ApJ, 520, 54
Kobayashi, S., Piran, T. & Sari, R. 1997, ApJ, 490, 92
Krumholz, M., Thorsett, S.E., & Harrison, F.A. 1998, ApJ, 506, L81
Kumar, P. 1999, ApJL, 523, L113
Li, H. & Fenimore, E.E. 1996, ApJ, 469, L115
Mao, S. & Mo, H.J. 1999, A&A, 339, L1
Mészáros , P., Rees, M.J., Wijers, R. 1999, New Astronomy, 4, 303
McBreen, B. et al 1994, MNRAS, 271, 662
Norris, J.P. et al. 1996, ApJ, 459, 393
Panaitescu, A. & Mészáros , P. 1999, ApJ, (astro-ph/9810258)
Panaitescu, A., Spada, M., & Mészáros , P. 1999 (PSM99), ApJL, 522, L10
Pendleton, G.N. et al. 1996, ApJ, 464, 606
Rees, M.J. & Mészáros , P. 1994, ApJ, 430, L93
Reichart, D.E. & Mészáros , P. 1997, ApJ, 483, 597
Totani, T. 1997, ApJ, 486, L71
Wijers, R. et al. 1998, MNRAS, 294, L7
Wijers, R. & Galama, T.J. 1999, ApJ, 523, 177

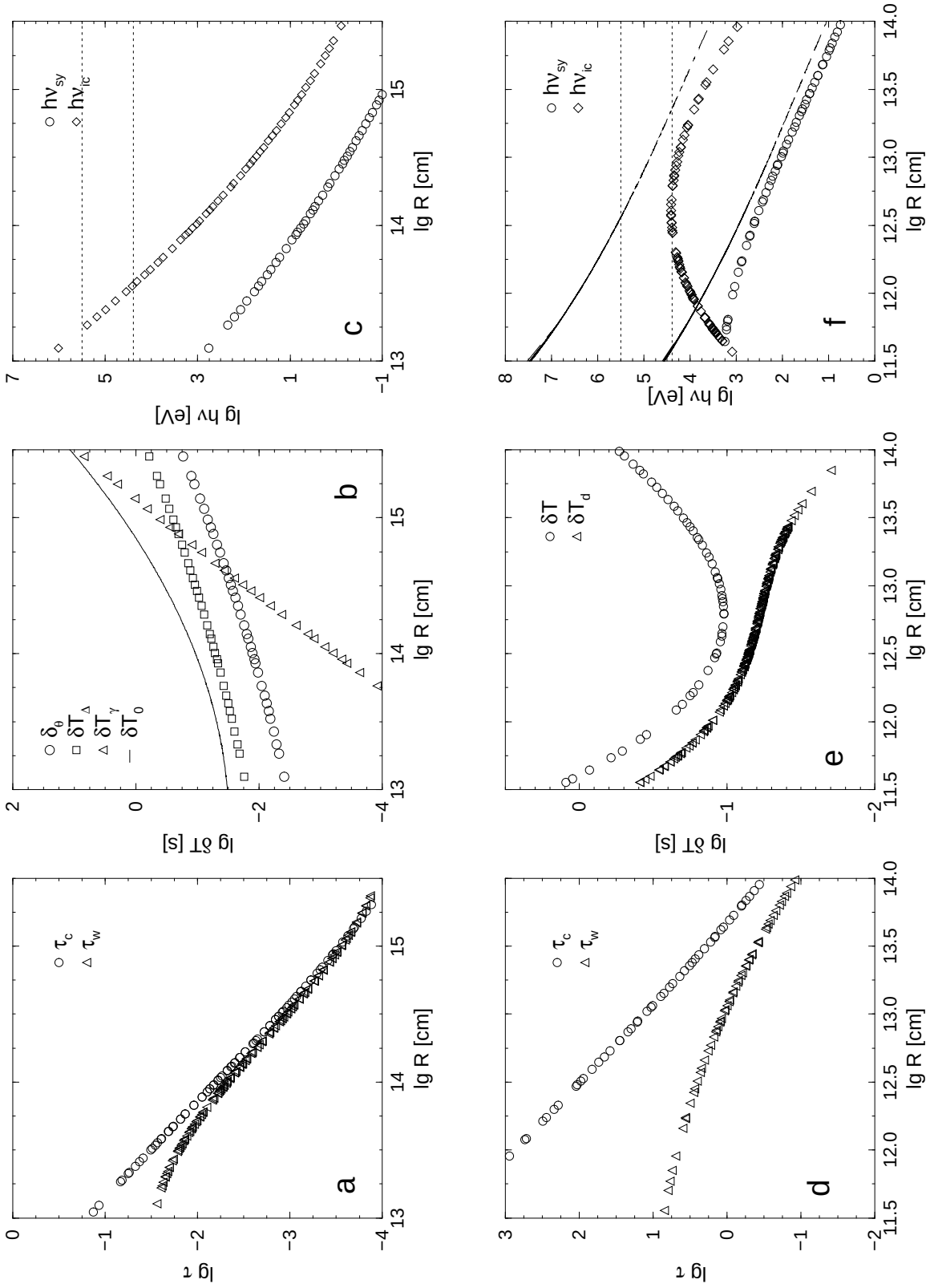


Fig. 1.— Upper panels: optically thin wind with $L_w = 10^{53}\,\mathrm{erg\,s^{-1}}$ and $30 < \Gamma < 1000$. Panel a shows the dependence on the collision radius R of the optical thickness τ_c for scattering on the cold electrons inside the emitting shell, and that of the rest of the wind (τ_w). Panel b illustrates the R-dependence of the pulse duration and of the terms that contribute to it; while graph c shows the R-dependence of the synchrotron and inverse Compton peak energies. Lower panels: optically thick wind $L_w = 10^{53}\,\mathrm{erg\,s^{-1}}$ and $5 < \Gamma < 300$. Graph d shows the R-dependence of τ_c and τ_w, graph e shows the evolution of the pulse duration $\delta T = \delta T_d + (\delta T_\theta^2 + \delta T_\Delta^2 + \delta T_\gamma^2)^{1/2}$ and the contribution of the diffusion time through the wind δT_d (i.e. excluding the emitting shell). Graph f shows the down-scattered synchrotron and inverse Compton energy peaks versus the collision radius. The dashed lines in panel f show the evolution of the synchrotron and inverse Compton peak before the down-scattering, and the dotted lines in panel c and f show the BATSE window. Parameters: $t_v = 0.02$ s, $t_w = 20$ s, $\epsilon_e = 0.25$, $\epsilon_B = 0.1$, $\zeta_e = 1$, burst redshift $z = 1$. Only a small fraction of the total number of pulses is shown; the density of the points illustrates the radius distribution. The curves shown are log-log space fits for the most efficient pulses. The actual values are scattered around the fit.

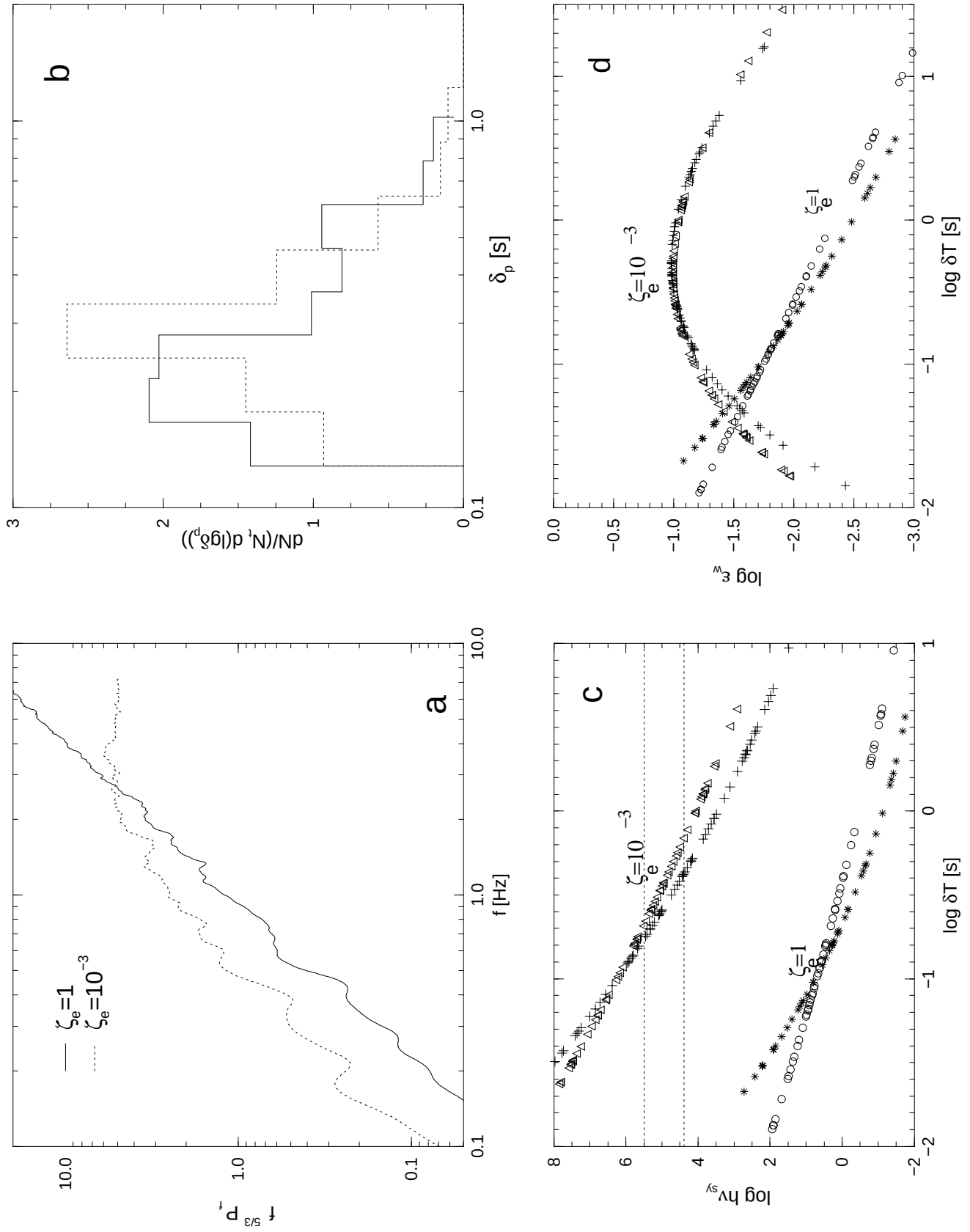


Fig. 2.— Effect of the injection fraction ζ_e on the burst PDSs (panel a), distribution of interval between peaks (panel b) for $N_t \sim 130$ peaks, energy of the synchrotron spectrum peak (panel c), and window efficiency (panel d). Parameters: $L_w = 10^{52}\,\mathrm{erg\,s^{-1}}$, $\Gamma_m = 30$, $\Gamma_M = 800$, other parameters are as for Figure 1. Panels c and d show log-log space polynomial fits, illustrating thus only the trends. The RS emission is represented with circles and triangles, while the FS one is shown with crosses and stars.

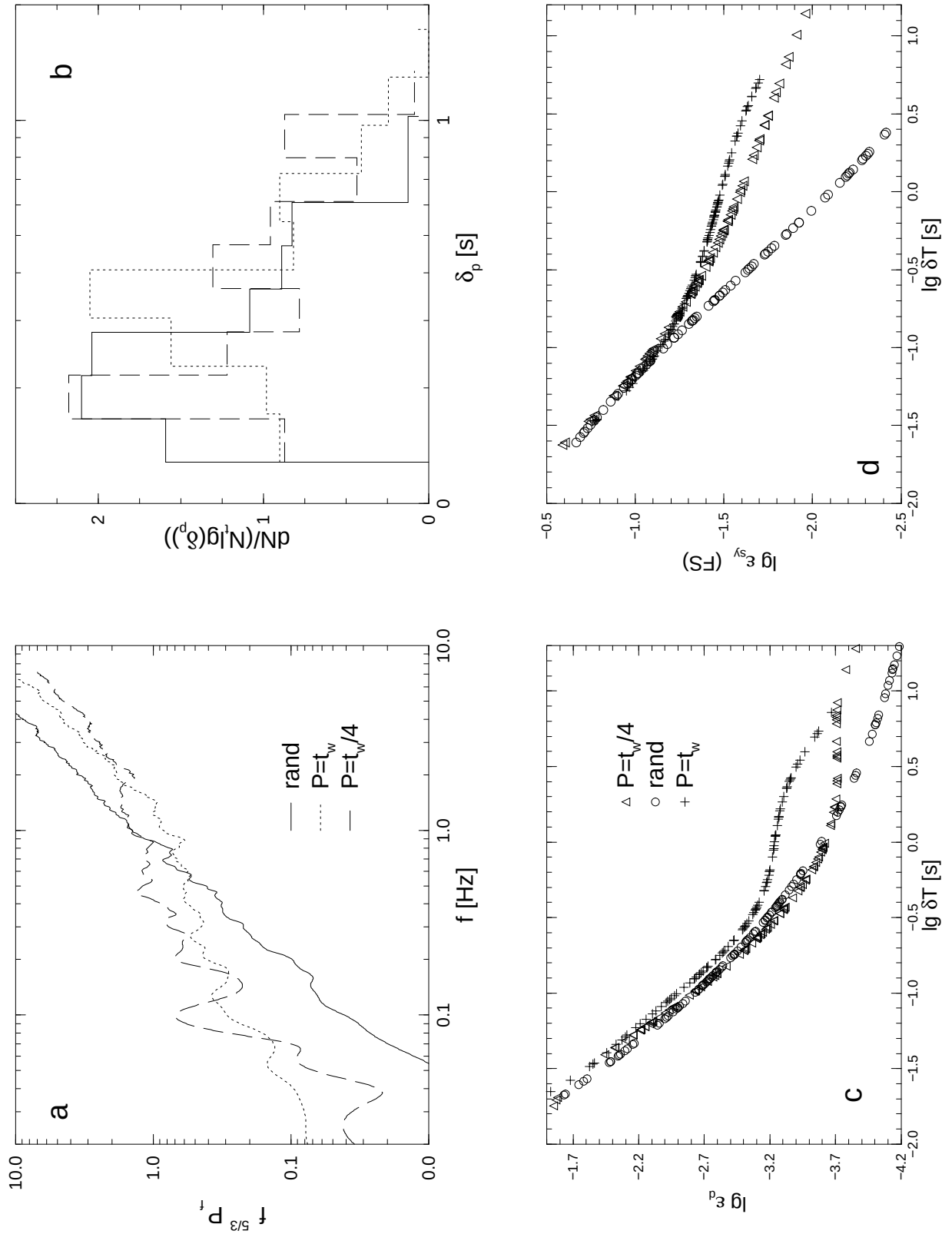


Fig. 3.— Effect of a modulation of the wind ejection. Panels a and b show a comparison between the PDSs and the δ_p distributions for an uniform wind (solid line), and a square-sine modulated ejection with period t_w (dotted line) and $t_w/4$ (dashed line). Parameters: $L_w = 10^{52}\,\mathrm{erg\,s^{-1}}$, $\Gamma_m = 30$, $\Gamma_M = 1000$, other parameters are as for Figure 2. Lower panels: the dependence of the dynamical efficiency (panel c), and FS synchrotron efficiency (panel d) versus the pulse duration.

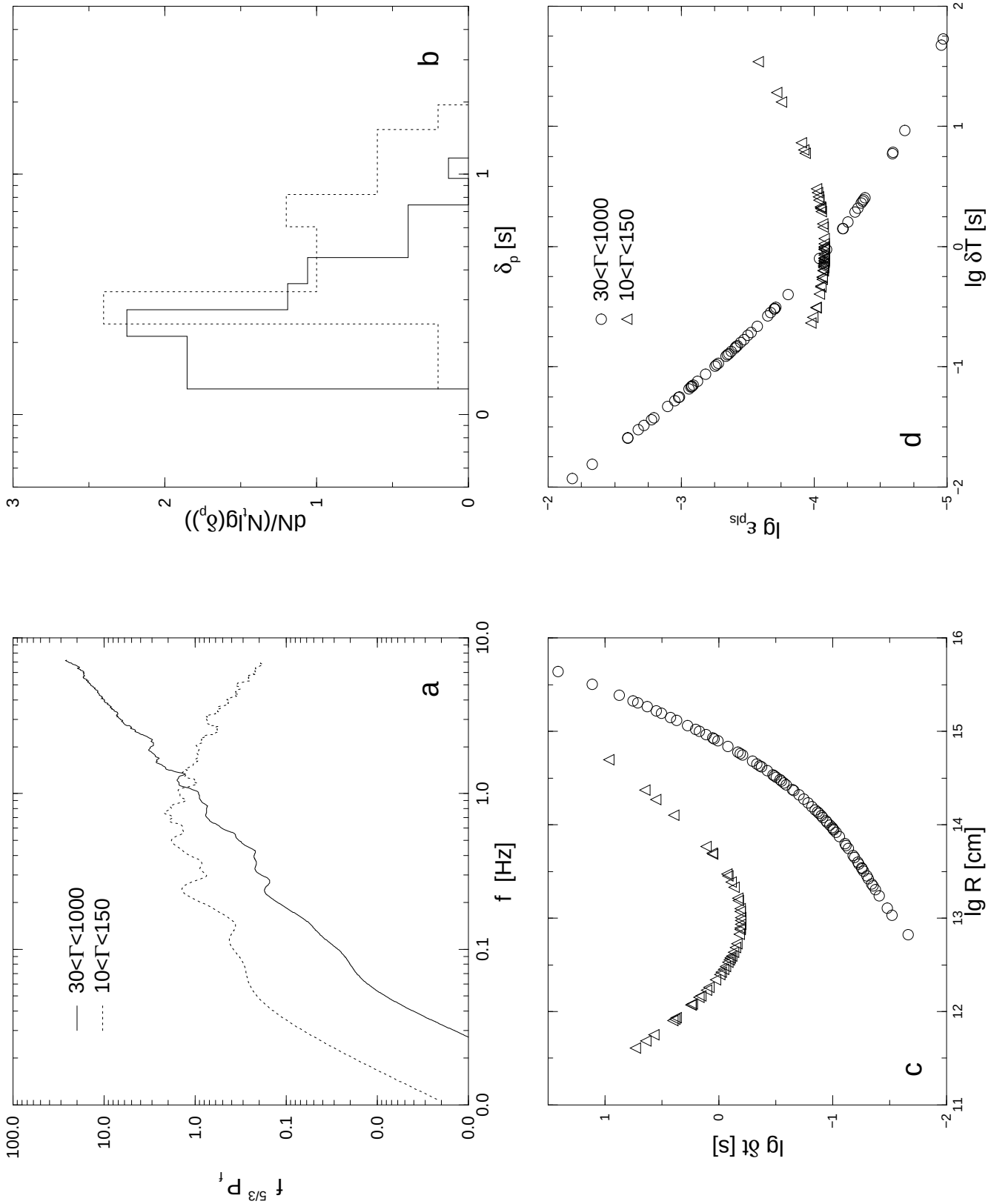


Fig. 4.— Effect of the optical thickness. Panels a and b show a comparison between the PDSs and the distributions of δ_p for an optically thin wind with $30 < \Gamma < 1000$ ($N_t = 70$ peaks), and an optically thick one with $10 < \Gamma < 150$ ($N_t = 40$ peaks). $L_w = 10^{53}\,\mathrm{erg\,s^{-1}}$, other parameters are as for Figures 2 and 3. The dependence of δT on the collision radius and of the pulse 50–300 keV fluence on δT are shown in panels c and d respectively, for the optically thick (triangle) and thin (circle) winds. The pulse fluence is the fraction of the total fluence in the light curve carried by each pulse.

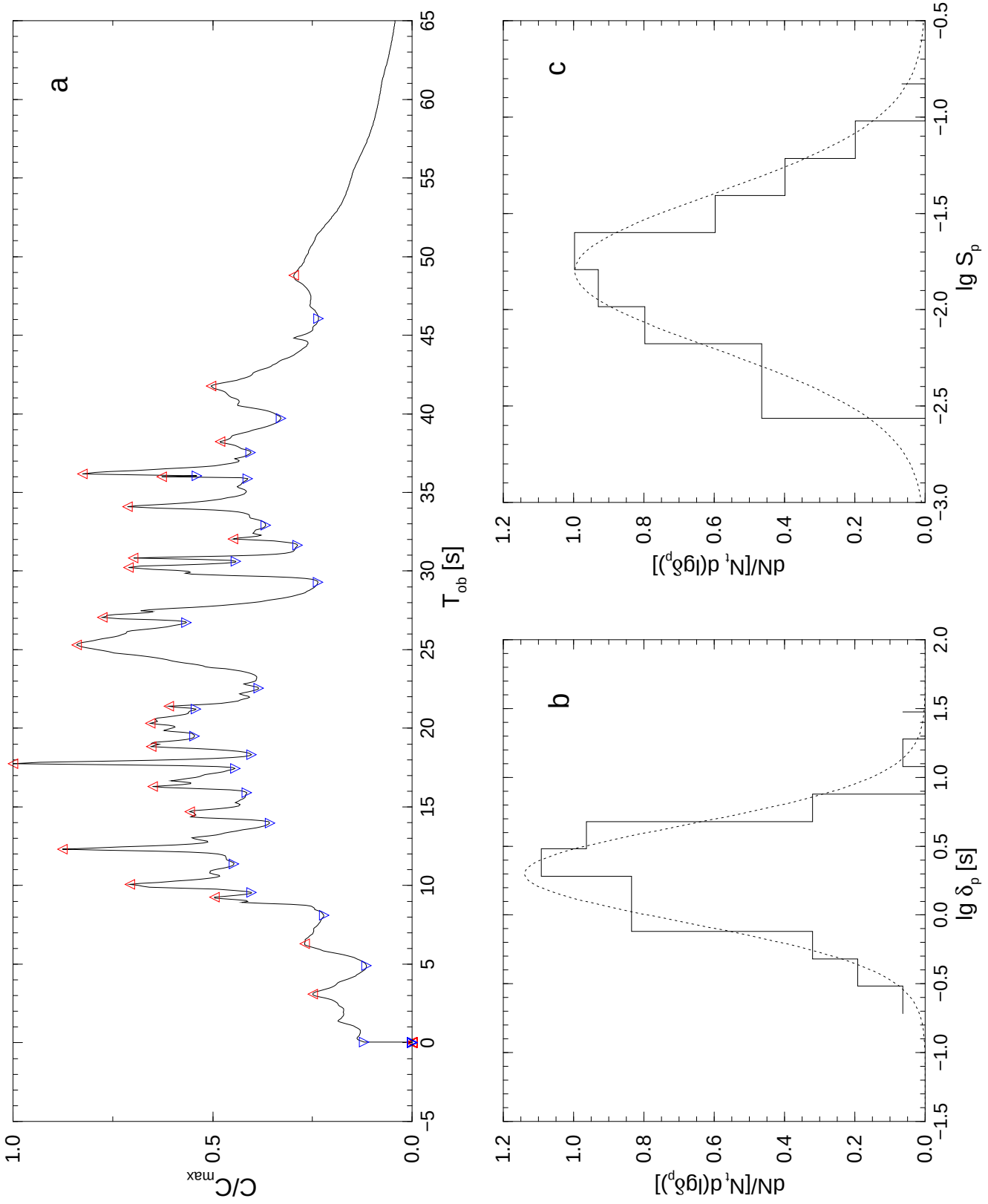


Fig. 5.— Top panel: light-curve for a modulated wind with $P = t_w$ and $\Gamma_m = 5$, $\Gamma_M = 150$, $L_w = 2 \times 10^{52}\,\mathrm{erg\,s^{-1}}$, $t_v = 25$ ms, $t_w = 30$ s, $z = 1$, $\zeta_e = 0.1$, $\epsilon_e = 0.25$, $\epsilon_B = 0.1$. The photon flux is normalized to its highest value. The triangle the peaks (38) and the valleys selected with the PFA ($N_{var} = 0.1$). Bottom: the distributions of the interval δ_p between peaks (b) and of the peak fluence S_p (c), the latter representing the fraction of the total fluence between two consecutive valleys. The distributions are calculated for four bursts with identical ejection features and wind parameters, total numbers of peaks is 80. The log-normal distributions that fit best the numerical results are shown with dotted curves.

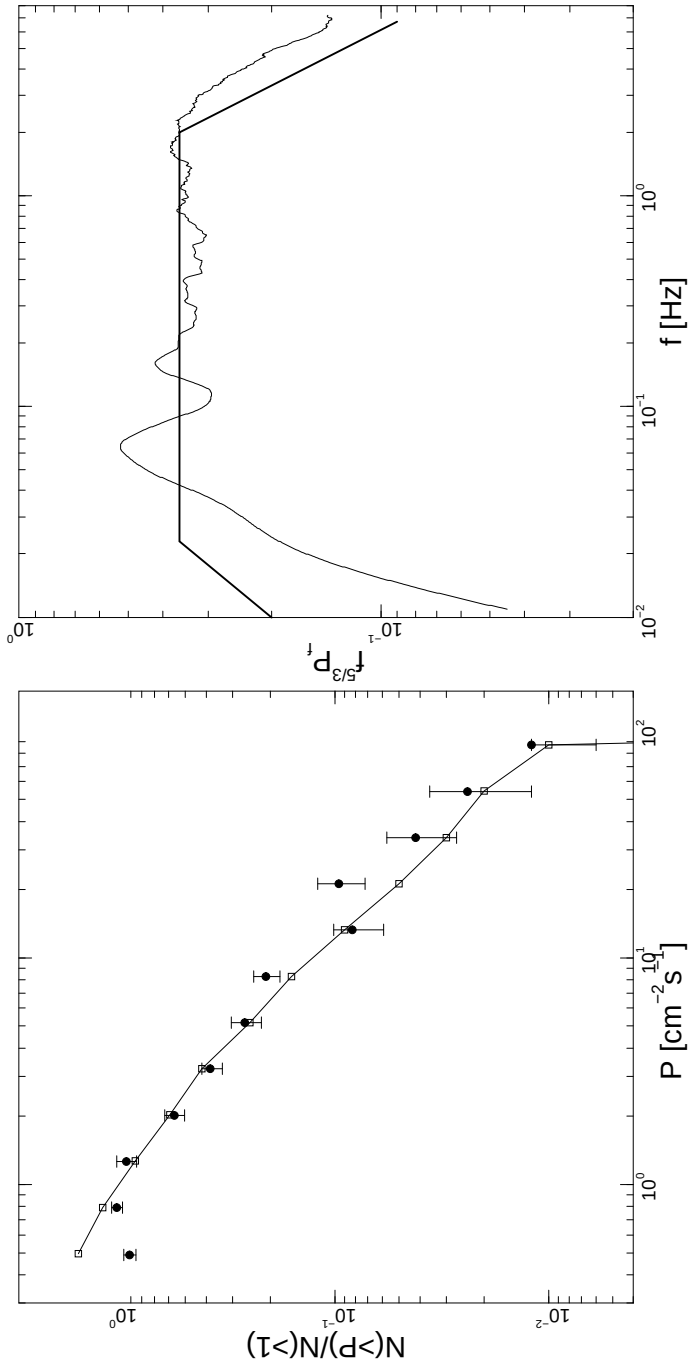


Fig. 6.— Left panel: intensity distribution of simulated bursts (open squares) compared to that of the observed ones, taken from Pendleton et al. (1996) (filled circles). Both distributions are normalized to the number of bursts brighter than $1\,\gamma\,\mathrm{cm}^{-2}\mathrm{s}^{-1}$. Right panel: the averaged PDS of the simulated bursts, compared with the shape of the PDS (thick line) determined by BSS98 for real bursts. The average is done over 112 bursts with a square-sine modulated wind of random period between $t_w/4$ and t_w. Parameters: $L_m = 2 \times 10^{52}\,\mathrm{erg\,s}^{-1}$, $L_M = 100 L_m$, $\beta = 2$, $D = 3$, $t_w = 30$ s, $t_v = 25$ ms, $\epsilon_e = 0.25$, $\epsilon_B = 0.1$, $\zeta_e = 0.1$, $\Gamma_m = 5$, $\Gamma_M = 150$, $D = 3$.